Catalysis Communications 175 (2023) 106622

Contents lists available at ScienceDirect

Catalysis Communications

journal homepage: www.elsevier.com/locate/catcom

Iron supported on beaded carbon black as active, selective and stable catalyst for direct CO_2 to olefin conversion

Stephan E. Schultheis [a,b], Felix Herold [c], Ezra S. Koh [a], Niklas Oefner [a], Maximilian Hungsberg [a], Alfons Drochner [a], Bastian J.M. Etzold [a,*]

[a] Technical University of Darmstadt, Department of Chemistry, Ernst-Berl-Institut für Technische und Makromolekulare Chemie, 64287 Darmstadt, Germany
[b] Technical University of Darmstadt, Darmstadt Graduate School of Excellence Energy Science and Engineering, 64287 Darmstadt, Germany
[c] Norwegian University of Science and Technology, Department of Chemical Engineering, 7491 Trondheim, Norway

ARTICLE INFO

Keywords:
Fischer-tropsch-synthesis
CO_2
Olefins
Carbon black
Iron

ABSTRACT

The Fischer-Tropsch-to-Olefins process allows to convert waste stemming CO_2 with green hydrogen to olefins. Iron can catalyse both core reactions: 1) reverse-water-gas-shift as well as 2) Fischer-Tropsch. Carbon supported catalysts were reported to be highly attractive in this context, but until now mainly non technically applicable research carbons like nanotubes or ordered mesoporous carbons were studied and long term stability studies are missing. Here, beaded carbon blacks, were studied as available and inexpensive support materials for Fe catalysts in CO_2-based FTO. The most promising support yielded selectivities towards olefins of almost 40% and showed for 170 h high stability.

1. Introduction

Lower Olefins (C_2-C_4) are indispensable intermediates in the chemical industry. [1] Approximately 20% of the yearly production revenue of the chemical industry is related to the olefin-based polymer industry. [2] Traditionally, olefins are produced via steam cracking of fossil feedstocks, like crude oil. [1] Due to the growing social and political awareness regarding sustainable production, non-fossil based production routes and the shift towards a circular economy gain great interest. [3,4] While part of the olefine based polymers can be recycled mechanically [5] a large portion still needs to be recycled by other means. [6] Direct chemical recycling to the olefin monomers is more or less impossible as selective breaking of the C—C bond and dehydrogenation is difficult. [7] A possible way to close the carbon cycle is i) gasification or incineration of the polymer waste and ii) synthesis of ethylene and propylene through hydrogenation of the resulting CO/CO_2 or solely CO_2 streams. [8] While the incineration of plastic waste is commercialized [9] and recently the gasification of these waste is studied intensively [10,11], the synthesis of Olefines from the CO/CO_2 streams remains the more critical challenge in this carbon cycle. Direct electrochemical reduction of CO/CO_2 to ethylene is an attractive process but still from a technical point of view not mature enough. Methanol synthesis and subsequent Methanol-to-Olefin (MTO) conversion is a possible route, while for the MTO process no large-scale production plant with a capacity of >1 MTPA is existing. The Fischer-Tropsch-Synthsis (FTS) in contrary is commercialized on big scales and it is known that the product selectivity for CO as feedstock can be tuned towards high olefine yields and in a single process. [1,12] Fischer-Tropsch-to-Olefins (FTO) can thus be an important, scalable and readily available process to close the carbon cycle for polypropylene and polyethylene recycling. CO_2 as feedstock, in combination with green hydrogen, would be especially interesting, as it cannot only stem from plastic waste incineration, but also other sustainable resources as well as from direct air capture. [3]

As CO_2 is not converted into Fischer-Tropsch-products directly, the reverse water-gas shift reaction (RWGS) to CO has to be carried out prior. The combination of this endothermic equilibrium reaction and the highly exothermic Fischer-Tropsch synthesis (FTS) can be realized either in two separate or in one combined reactor unit. Due to their opposite reaction enthalpies and process intensification aspects, the direct heat integration is one main advantage of coupling both reactions in one reactor. Additionally, as CO is converted to FTS-products in a series of irreversible consecutive reactions, a high CO_2 conversion by RWGS can be obtained even at low temperatures. However, the coupling of RWGS and FTS demands a catalyst system exhibiting activity for both the shift-reaction and the FTS, which is met by using Fe as an active metal. [4]

In this context, especially carbon supported iron catalysts are of

* Corresponding author.
E-mail address: bastian.etzold@tu-darmstadt.de (B.J.M. Etzold).

https://doi.org/10.1016/j.catcom.2023.106622
Received 25 January 2023; Accepted 3 February 2023
Available online 6 February 2023

increasingly growing interest. [13–15] Compared to the traditionally used oxidic support materials, such as SiO_2 and Al_2O_3, iron species on carbon materials prove to be reducible more easily, since there is no strong metal support interaction (SMSI). This facilitates the conversion of Fe species into FT-active carbides, as the carbidisation of elemental iron is facilitated on carbon supports. [16,17] Despite the less pronounced interactions between support and active metal, carbon-supported iron systems, as demonstrated by the use of carbon nanotubes (CNT) as support, showed excellent resistance to sintering. [18,19]

Regarding the utilization of carbon supported Fe in a CO_2 based FTO process, *Oschatz* et al. reported sulfur and sodium as promising promotors for the production of olefins using ordered mesoporous carbon (CMK-3) as support route. [20–23] They found that the undesired methane formation is inhibited by sulfur doping, while the desired β-hydride elimination to short chained olefins is preferred at the same time. Addition of sodium supports chain growth and reduces selectivity to methane while inhibiting olefin hydration to paraffins. [24]

Most of the existing studies dealing with Fe/C-catalysts in the FTS were carried out using research carbon materials like CNT's or CMK-3. Facing the challenges of an industrial FTS process, these materials reveal disadvantages for commercialization of derived catalysts like expensive and complicated synthesis, as well as handling on the industrial scale of these small sized powdered materials and the resulting severe pressure drop for technical fixed bed reactors. Also, so far, results are mainly presented for some hours time on stream and rarely long term stability studies for several hundred hours. Overall, both hinders an application of Fe/−catalysts in FTO strongly.

The following study presents the use of beaded carbon blacks (CBs) as support for iron based CO_2-FT catalyst. CB represents a material which is widely available in industrial scale at low price with additional formulation procedures to reduce pressure drop for fixed bed reactors e.g. through beading also being carried out on an industrial scale. Commercial beaded CBs varying in properties (e.g. specific surface areas from 36 $m^2 \cdot g^{-1}$ to 380 $m^2 \cdot g^{-1}$) were employed for catalyst synthesis. The catalyst performance in direct olefin synthesis for CO_2 hydrogenation was assessed and for the most promising catalyst a long-term study proved stability for 170 h time on stream.

2. Materials and methods

2.1. Catalyst preparation

Five commercially available beaded Carbon Blacks (Orion Engineered Carbons: Printex G, Printex 35, Printex 60, Printex 85, Printex 90) were used as supports in this study. The preparation strategy was modified according to *Oschatz* et al. [15] Carbon supported catalysts were prepared by incipient wetness impregnation, using a solution of ammonium-iron-citrate (1.787 g; 16.5–18.5% Fe; Acros Organics), tri-sodium-citrate dihydrate (0.038 g; 99+ %, Fisher Scientific), and iron sulfate heptahydrate (0.026 g; 99+ %; Acros Organics) in 6 mL bidistilled water. Concentrations were chosen so that a loading of 10 wt % Fe, 0.3 wt% Na and 0.1 wt% S with respect of the carbon support results. 3 g of dried carbon support (100 °C over night) was impregnated with this solution in six to eight steps depending on the capacity of the support material. Every impregnation step was followed by a two hour drying step at 100 °C combined with the homogenization of the sample in an achate mortar. After the last drying step, the raw catalyst was calcinated in a tube furnace for 5 h at 500 °C under constant nitrogen flow at atmospheric pressure. This catalyst is referred to as pristine catalyst.

2.2. Catalyst characterization

Optical emission spectrometry with inductively coupled plasma (ICP-OES, Optima 2000DV (Perkin Elmer)) was used to determine the loading of Fe, Na and S on the carbon supports. Sample preparation included the oxidation of the carbon support at 500 °C in a muffle furnace, followed by aqua regia digestion of the residues. N_2-physisorption measurements (Quadrasorp-MP-30 (Quantachrome Instruments)) are carried at −196 °C, with samples degassed at 350 °C and 0.1 mbar for 18 h. The multi-point Brunauer-Emmett-Teller method (MBET) is used to determine the specific surface area. [25] The pore volume is determined by means of density functional theory (DFT) using the adsorption isotherm. Oil adsorption is used to determine the degree of branching of the carbon blacks studied. The determination is made by Orion Engineered Carbons according to ISO 4656 respectively ASTM D 2414 utilizing dibutyl phthalate as adsorbate. [26] TPD-MS was carried out in a STA 409 PC Luxx thermo-balance (NETZSCH) coupled with an online mass spectrometer (Omnistar, Pfeiffer Vacuum GmbH). For this purpose, 150 mg of the carbon black were initially heated to 80 °C at a flow rate of 30 NmL min^{-1} He with a heating rate of 5 °C min^{-1} and dried for 30 min. The sample was then heated from 80 °C to 1000 °C at a heating rate of 5 °C min^{-1}. X-Ray diffraction (XRD) measurements have been performed in a Stadi-P (Stoe GmbH) using a Cu-Kα,1-source. Elemental analysis was carried out in a Vario EL III analyzer (Elementar Analysensysteme GmbH). All samples were measured five times. The determination of the primary particle size was carried out by means of dynamic light scattering by Orion Engineered Carbons. [27] The ISO 1125 respectively ASTM D 1506 standard was used to determine the ash content of the carbon blacks used by Orion Engineered Carbons. [28] Scanning transmission electron microscopy (STEM) was carried out in a JEM 2100F (JEOL) with an accelerating voltage of 200 kV and a spot diameter of 0.7 nm. STEM images were used for the determination of the iron particle size distribution, by analyzing a minimum of 50 particles per sample. Scanning electron microscopy (SEM) was carried out using a Philips XL30 FEG electron microscope with an acceleration voltage of 10–15 kV. X-ray diffraction (XRD) was performed using a Rigaku Miniflex exquipped with a D/tex Ultra detector (CuKα, 40 kV, 0.03 mm Ni-filter). Temperature programmed reduction (TPR), CO-Chemisorption as well as CO- and CO_2-temperature programmed desorption (TPD) were carried out in a 3Flex (Micromeritics) chemisorption unit. TPR is performed up to 400 °C with a heating rate of 5 °C min^{-1} using 0.5% H_2 in Argon. Following an evacuation, static CO-chemisorption is performed at 30 °C between 100 mbar and 800 mbar. Afterwards CO-TPD is realized between 30 °C and 400 °C obtaining a heating rate of 5 °C min^{-1}. Next a second TPR is performed and the sample is again evacuated. After the CO_2-saturation of the sample using 4% CO_2 in He at 30 °C, CO_2-TPD is performed at a temperature up to 600 °C using a heating rate of 5 °C min^{-1}.

2.3. Catalyst activity measurement – support variation

Catalyst reduction and CO_2-FTS activity measurements were carried out in the same u-shaped fixed bed reactor. 0.5 g of the pristine catalyst were placed into the reactor and fixed with the aid of two glass wool plugs. Catalyst reduction was carried out at 300 °C for 5 h at 30 bar using pure hydrogen. For FTS, a premixed H_2:CO_2-mixture (3:1 mol mol^{-1}) was used as feed at a mass flow of 0.03 g min^{-1} (GHSV = ~8000 h^{-1}). 325 °C were set as standard temperature. Carbon monoxide and carbon dioxide were detected via FT-IR (Bruker alpha), hydrocarbons were analysed in a Shimadzu GC-2014 gas chromatograph equipped with two FID's. Separation of C_1-C_6-hydrocarbons took place at a Rt-QS-BOND Plot column (Restek) while higher hydrocarbons were separated at a Rtx-column (Restek). Resulting σ_i values represent the fraction of the respective substance class i of the total amount of hydrocarbons and are standardized to one. All conversions, selectivities and product distributions shown result from the mean value of three measurements after 30 h TOS.

2.4. Long-term-stability measurement

For the long-term measurement,1.5 g of the pristine catalyst (Printex

60) and 3.0 g Printex 60 carbon black as inert dilution were placed into the reactor and fixed with the aid of two glass wool plugs. Catalyst reduction was carried out at 300 °C for 5 h at 30 bar using hydrogen in helium (1:2 mol mol^{-1}). A stoichiometric H_2:CO_2:CO-mixture (2.5:0.5:0.5 mol mol mol) was used for preconditioning of the catalyst for the first 48 h TOS at 325 °C. After preconditioning, the feed was set to a stoichiometric H_2:CO_2-mixture (3:1 mol mol^{-1}) using 80.7 NmL min^{-1} H_2 and 3.2 g min^{-1} CO_2 (GHSV = ~3200 h^{-1}). Product analytics were performed using an Agilent GC6890N gas chromatograph equipped with one FID and one TCD. Separation of C_1-C_3-hydrocarbons as well as CO and CO_2 took place at a Rt-QS-BOND Plot (Restek) column and a Rt-Alumina (Restek) column while higher hydrocarbons were separated at a Rtx-column (Restek). Resulting σ_i values represent the fraction of the respective substance class i of the total amount of hydrocarbons and are standardized to one.

2.5. Calculations

Carbon dioxide (X_{CO2}) conversion is calculated dividing the difference between the initial quantity ($\dot{n}_{0,CO_2}$) and the resulting quantity of carbon dioxide ($\dot{n}_{CO_2}$) through the initial quantity (eq. 1).

$$X_{CO2} = \frac{\dot{n}_{0,CO_2} - \dot{n}_{CO_2}}{\dot{n}_{0,CO_2}} \quad (1)$$

Selectivity to carbon monoxide ($S_{CO,CO2}$) build out of carbon dioxide is calculated dividing the resulting quantity of CO ($\dot{n}_{CO}$) through the difference between the initial quantity ($\dot{n}_{0,CO_2}$) and the resulting quantity of carbon dioxide ($\dot{n}_{CO_2}$) (eq. 2).

$$S_{CO,CO2} = \frac{\dot{n}_{CO}}{\left(\dot{n}_{0,CO_2} - \dot{n}_{CO_2}\right)} \quad (2)$$

Selectivity to hydrocarbons ($S_{HC,CO2}$) build out of carbon monoxide is calculated dividing the product of the resulting quantity of HC ($\dot{n}_{HC}$) and its number of carbon atoms ($N_{C,\ HC}$) through the difference between the initial quantity ($\dot{n}_{0,CO_2}$) and the resulting quantity of carbon dioxide ($\dot{n}_{CO_2}$) (eq. 3).

$$S_{HC,CO2} = \frac{\dot{n}_{HC} \bullet N_{C,HC}}{\dot{n}_{0,CO_2} - \dot{n}_{CO_2}} \quad (3)$$

Yield of product P ($Y_{P,CO2}$) is calculated multiplying the selectivity of product P with the carbon dioxide conversion (eq. 4).

$$Y_{P,CO2} = S_{P,CO_2} \bullet X_{CO_2} \quad (4)$$

Using the selectivities for hydrocarbons ($S_{HC,r}$), the product fractions $\sigma_{HC,r}$ are determined. This calculation (eq. 5) is based on the normalization of the product spectrum and serves the separate consideration of the resulting FT product distribution neglecting the WGS equilibrium.

$$\sigma_{HC,r} = \frac{S_{HC,r}}{\sum_{HC} S_{HC,r}} \quad (5)$$

Since the focus of this work is on the production of short-chain olefins, the olefin fraction in the C_2-C_6 fraction of the product spectrum is introduced as a further measure (eq. 6).

$$C_2 - C_6 - \text{olefin fraction} \hat{=} \frac{x_{C_2-C_6,\text{olefins}}}{x_{C_2-C_6,\text{total}}} \quad (6)$$

Using the logarithmic expression shown in eq. 7 and via linear regression, the chain growth probability α is determined graphically. For this purpose, log x_{HC} is plotted against the carbon number $N_{C,HC}$.

$$log x_{HC} = N_{C,HC} \cdot log\alpha + log\frac{(1-\alpha)}{\alpha} \quad (7)$$

3. Results and discussion

3.1. Carbon support properties and characterization of pristine catalysts

Carbon blacks are known to be hierarchically build from primary particles, forming stable aggregates and loose agglomerates. The employed carbon blacks exhibit a wide variety of properties, owing to variations in their microstructure. As shown in Fig. 1A, all carbon blacks exhibit different primary particle sizes. [27] Starting with Printex G, the primary particle size decreases from 51 nm to 14 nm for Printex 90. The aggregates built from these primary particles were characterized by oil adsorption carried out with dibutyl phthalate (DBP), with the resulting DBP number representing a measure for the degree of branching (Fig. 1A). [27] With 48 mL_{DBP} 100 g^{-1} and 42 mL_{DBP} 100 g^{-1}, Printex 35 and 85 have by far the lowest DBP number, and exhibit therefore the most linear structure. Printex 60 with 115 mL_{DBP} 100 g^{-1} is the carbon black with the highest degree of branching. Due to the different primary particle sizes and structuring of the aggregates, varying textural properties result. The N_2-physisorption isotherms (Fig. 1B) of Printex G, 35 and 60 represent isotherms of type III according to IUPAC nomenclature. They include almost no uptake in the relative pressure range of 0 to 0.1, and furthermore lack desorption hysteresis indicating the absence of meso- and microporosity. Since the majority of nitrogen uptake occurs at relative pressures above 0.8, and no plateau could be observed, macroporosity is dominant in these materials. In contrast, the isotherms of Printex 85 and Printex 90 show a desorption hysteresis (type H3) and a low nitrogen uptake in the relative pressure range of 0–0.1 can be observed, resulting in a classification as a mixture of Type II and Type IV. [25] The specific surface area (SSA, determined by BET) increases with decreasing primary particle size from 36 m^2 g^{-1} (Printex G) to 380 m^2 g^{-1} (Printex 90). With high probability, the SSA results from the geometric surface of the particles, with particle interstices as the origin of porosity. In consequence, the degree of branching plays an important role, as is illustrated by Printex 85 and Printex 90, which both have a similar primary particle size, but a clearly different structuring and thus a very different *SSA*.

These findings are clearly supported by scanning electron microscopy (SEM) and transmission electron microscopy (TEM, Fig. 2). SEM imaging of Printex G and Printex 90 illustrates the different morphologies that result from the difference in primary particle size. Printex G, which exhibits a large primary particle size of 54 nm, shows clear macroporosity at the agglomerate level, while Printex 90, which has an average primary particle diameter of 14 nm, appears to largely lack porosity in the µm range (Fig. 2A, B). TEM imaging shows that the aggregates of Printex G and Printex 90 exhibit clear differences in terms of particle interstices that reach up to several tens of nanometers for Printex G, while they are significantly smaller in case of Printex 90 (Fig. 2C, D).

In addition to their structure, the composition of the carbon black supports is of interest, which can be described by the carbon content, the amount of ash and amount of volatile components (Fig. S1). Carbon content of the different carbon blacks ranges from 97 wt% for Printex 85 to up to 99.7 wt% for Printex 35. In addition to the lowest carbon content, Printex 85 reaches the highest values in case of volatiles (1.2 wt %) and ash (0.8 wt%). Volatile components are often present in the form of oxygen surface groups on the carbon surface. In order to be able to identify carbon surface oxides, temperature-programmed desorption measurements with coupled mass spectrometry (TPD-MS) were carried out (Fig. S2). During TPD to 1000 °C, Printex 35 shows no detectable mass loss, while the largest loss (1.7 wt%) is observed in case of Printex 85. Regarding the detected CO, CO_2 and H_2O emission profiles it must be emphasised that the interpretation must be done with caution due to the very low amount of surface groups on the soot surface. In addition, due to the wide temperature ranges of the desorption of different surface species, it is generally difficult to make assignments. For Printex 85, three H_2O desorption maxima can be observed at 180 °C, 300 °C and

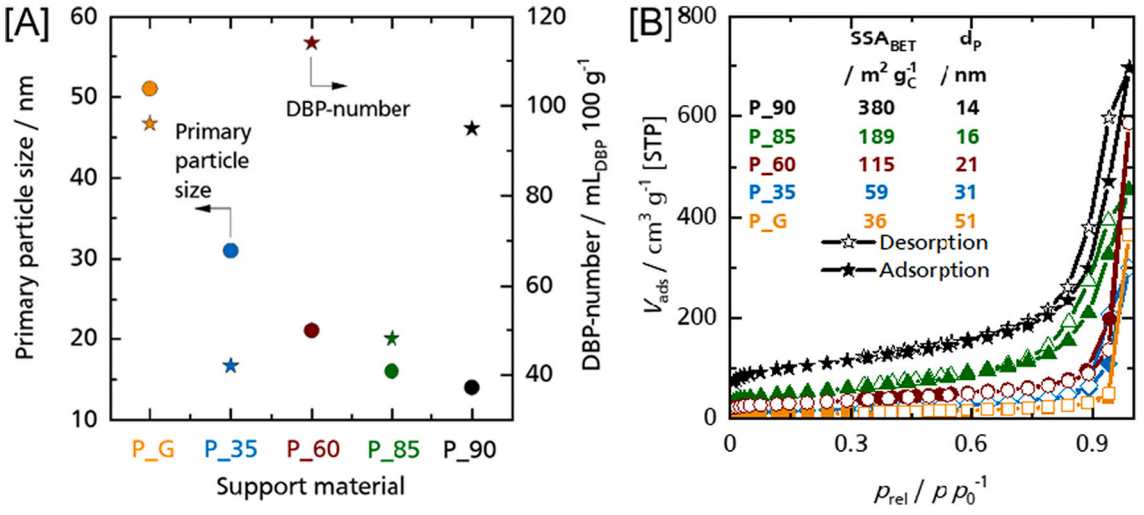

Fig. 1. (A) primary particle sizes as well as DBP-numbers resulting from of oil adsorption measurements for all pristine carbon black catalyst supports. (B) N_2 adsorption isotherms at 77 K and specific surface areas (BET).

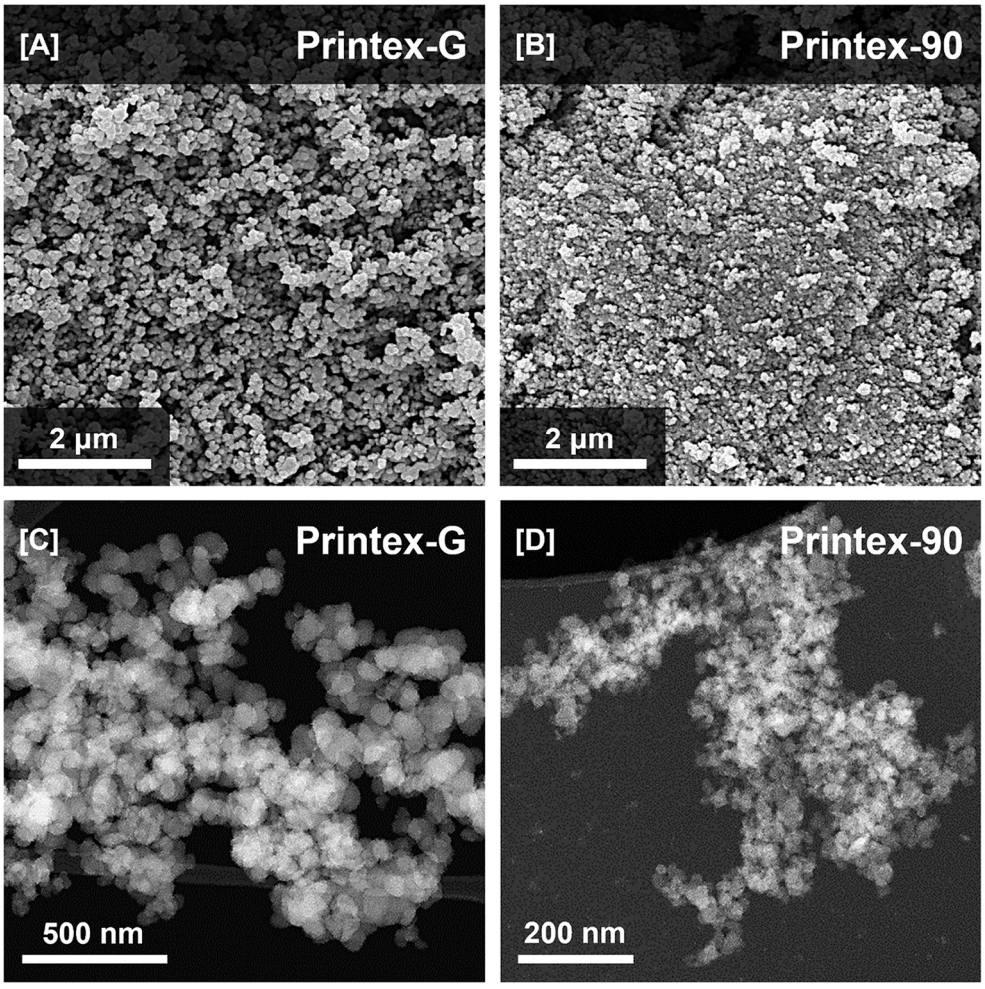

Fig. 2. Secondary electron micrographs of the pristine (A) Printex G and (B) Printex 90 carbon blacks. Annular darkfield transmission electron micrographs of the pristine (C) Printex G and (D) Printex 90 carbon blacks.

710 °C. The detection of water might be assigned to condensation reactions, for example of two hydroxyl groups to an ether. The CO_2 emission profile shows desorption maxima in comparable temperature ranges. CO_2 emission in the range between 200 °C and 400 °C can be assigned to the decarboxylation of carboxylic acids and anhydrides, while high temperature CO_2 evolution (>500 °C) indicates the decomposition of lactones. CO emission is detected above 600 °C. This desorption range is characteristic for the presence of hydroxyl groups,

ethers, ketones or aldehyde groups. [29–31]

The carbon-supported iron catalysts were prepared by incipient wetness impregnation (IWI). As described in detail in the experimental section, the target loading was 10 wt% iron (Fe), 0.3 wt% sodium (Na) and 0.1 wt% sulfur (S). Fe, Na and S loading was determined by means of optical emission spectroscopy with inductively coupled plasma (ICP-OES) (Fig. 3A). The mean loading of the samples was found to be 9.75 wt % (Fe), 0.66 wt% (Na) and 0.16 wt% (S). It should be emphasised that there are clear outliers in the form of the P_85-Fe/Na/S (sodium 0.93 wt %) and P_90-Fe/Na/S (sulfur 0.27 wt%) catalysts. On average, the iron loading is slightly below the target value of 10 wt%. At the same time, the sodium and sulfur loadings clearly exceed the respective target value. With regard to the sulfur loading, weighing error might play a role, but also the influence of sulfur impurities in the pristine carbon black is conceivable, since the industrial carbon blacks used are produced on the basis of crude oil. The sulfur content in the pristine carbon black determined by ICP-OES is up to 0.02 wt%. This form of contamination is also conceivable in the case of sodium loading. The sodium content in the pristine carbon black is <0.025% by weight. An important source of error arises regarding the sodium content in the sodium citrate dihydrate used as a precursor for Na loading. According to the manufacturer, this amounts to 16.5–18.5 wt%. In control samples examined by ICP-OES, the content was clearly higher at around 24 wt%.

The pristine carbon black and final catalyst were additionally characterized by X-ray powder diffraction (XRD) (Fig. S3). Due to the high content of amorphous domains in the samples, an intensive background noise can be observed. The diffractogram of the Printex 60 carbon black shows two significant reflections at diffraction angles of 25° and 43° that can be assigned to the 002 and 100 or 101 lattice planes of graphitic domains. [32] As expected, for the support loaded with iron, sodium and sulfur, additional reflexes appear, that are characteristic for iron oxides consisting of different species. Due to the very broad reflections, which may be caused by the small crystallite sizes of the supported iron oxide particles, an exact assignment of the reflections is not possible. The most dominant reflections are at 35°, 43° and 62°. These can be assigned to the 311, 400 and 440 reflections of magnetite (Fe_3O_4) [33] or the 111, 200 and 220 reflections of wüstite (FeO) [34]. The low symmetry of the reflexes at 35° and 43° is also an indication of the superposition of at least two reflections of different species. Furthermore, the reflex intensities of the powder diffractograms shown do not correspond to the reflex ratios of phase-pure Fe_3O_4 or FeO species. [35]

As a result of Fe, Na and S loading, changes in texture can occur resulting from the deposition of the active phase on the carbon blacks and from the restructuring of the agglomerates due to the water impregnation process. A comparison of the specific surface area and the pore volumes before and after Fe, Na and S loading is shown in Fig. S4. Both SSA_{BET} and V_{Pore} show comparable trends. Printex G and 35 supported catalysts show slight increases in SSA_{BET} and V_{Pore} (SSA_{BET}: P_G to P_G-Fe/Na/S (by 50% from 36 to 54 $m^2\ g^{-1}$), P_35 to P_35-Fe/Na/S (by 22% from 59 to 72 $m^2\ g^{-1}$); V_{Pore}: P_G to P_G-Fe/Na/S (by 66%

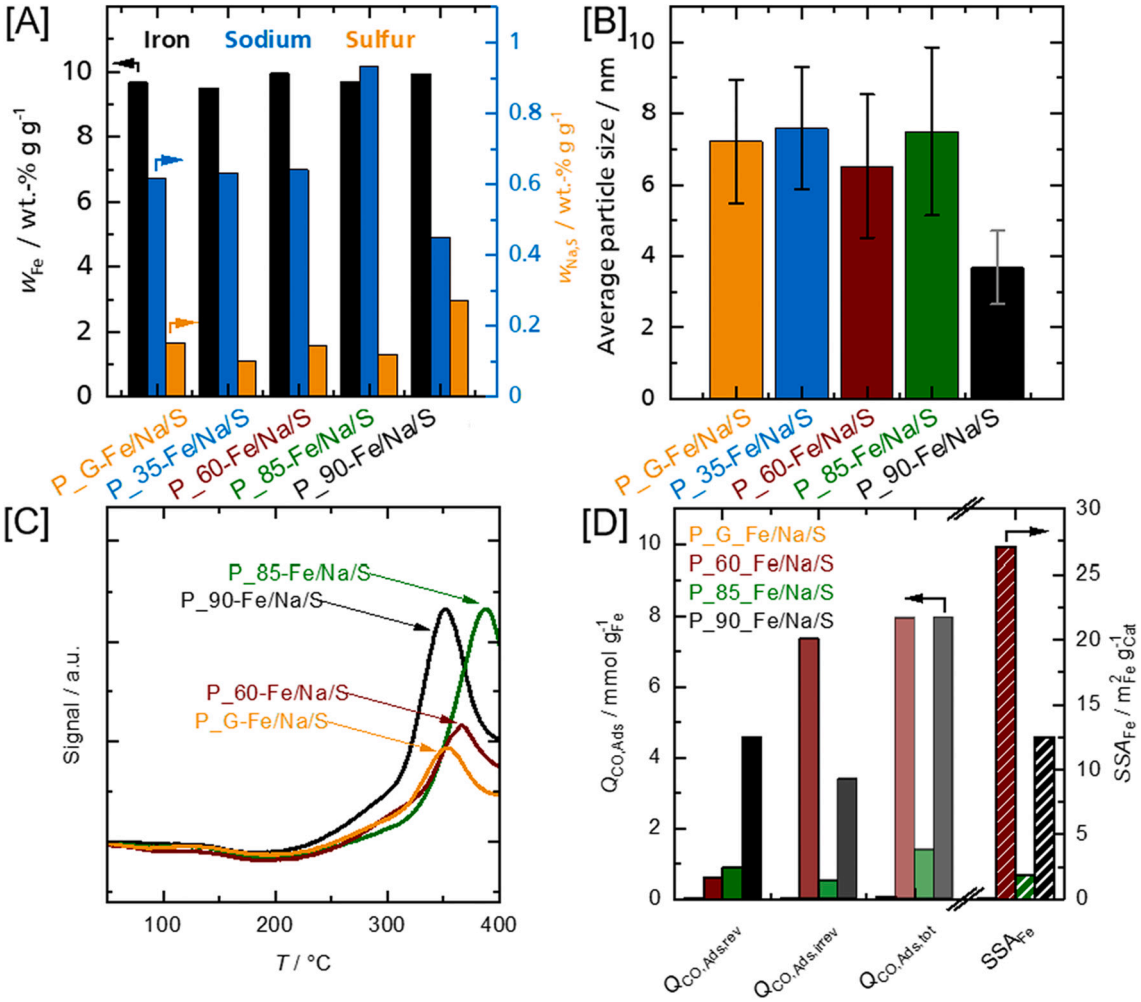

Fig. 3. (A) Loading of iron, sodium and sulfur determined by ICP-OES for all pristine catalysts. (B) Average iron particle sizes and resulting standard deviations. (C) H_2-TPR curves in the temperature range between 50 °C and 400 °C. (D) Specific iron surfaces (SSA_{Fe}) as well as the adsorbed CO-amounts resulting from static CO-chemisorption.

from 0.06 to 0.10 $cm^3\ g^{-1}$), P_35 to P_35-Fe/Na/S (by 69% from 0.16 to 0.27 $cm^3\ g^{-1}$)). P_60 and P_60-Fe/Na/S include almost constant SSA_{BET} (~116 $m^2\ g^{-1}$) as well as slightly increasing V_{Pore} (by 25% from 0.20 to 0.25 $cm^3\ g^{-1}$). The values of P_85 and P_90 behave differently, as the initial specific surface areas decrease significantly (P_85 to P_85-Fe/Na/S (by 23% from 195 to 150 $m^2\ g^{-1}$), P_90 to P_90-Fe/Na/S (by 24% from 389 to 297 $m^2\ g^{-1}$)). In addition to that, the loss regarding pore volume is also significant, especially for P_85-Fe/Na/S (by 47% from 0.47 to 0.25 $cm^3\ g^{-1}$).

Transmission electron microscopy was employed to determine the iron particle sizes distribution (Fig. 3B and Fig. 4). All materials show a narrow distribution of nanoscale iron oxide particles in the range of 2 to 15 nm. This is particularly evident from the low standard deviation of 2.4 nm in the case of P_35-Fe/Na/S. Fe particles larger than 20 nm were not found in any of the samples examined. The maximum of the Fe particle size distribution for P_90-Fe/Na/S is 3.7 nm. All other supports show average particle diameters in the range of 6.5 nm to 7.5 nm. These observations correspond well with results of *Oschatz* et al., who reported narrow size distributions of Fe particles deposited on CMK-3 and carbon black supported systems with comparable metal loadings and dopants. Average particle sizes were reported to be 5.58 nm and 4.2–4.7 nm for CMK-3 and carbon black supported catalysts, respectively, with standard deviations of 1.22 nm and 1.0 nm. [15,22]

H_2-TPR measurements (Fig. 3C) lead to comparable trends. All four examined samples include a broad reduction peak with a connected shoulder (Onset-Temperature ~ 200 °C). The peak temperatures lie in a range between 353 °C (P_G-Fe/Na/S and P_90-Fe/Na/S) and 388 °C (P_85-Fe/Na/S). *Chew* et al. and *Ma* et al. report two reduction peaks for Fe/CNT- respectively Fe/AC-systems in the same temperature range. The first peak between 200 °C and 300 °C is related to the reduction of Fe_2O_3 to Fe_3O_4. This would indicate that P_90-Fe/Na/S includes the highest amount of Fe_2O_3. The second peak between 300 °C and 400 °C can be assigned to the reduction of Fe_3O_4 to FeO. [36,37] A third reduction peak representing the reduction of FeO to Fe in the temperature range up to 700 °C is to be expected but is not investigated here. [37] The presence of a low-temperature shoulder due to the absence of sharply separated reduction peaks in the case of this study can be related to impoverishment effects due to the low H_2 concentration of 0.5%. The observed differences in the temperature of the H_2 consumption maxima and the corresponding peak intensities are most likely a consequence of differences in the metal support interactions between Fe/Na/S and the different carbon black supports. In this context it is well-known that support properties influence the reducibility as well as the ratio of FeO_x species that are obtained after calcination. [36]

To probe the influence of the carbon support on CO_2 and CO adsorption properties, CO- as well as CO_2-TPD was carried out. Reduced catalysts were used in this context, it should be noted, however, that due to instrumental limitations the reduction conditions differ from those used for the catalytic activity tests. Regarding CO_2-TPD of CO_2-saturated iron catalysts, studies of *Cheng* et al., *Xu, Wang* et al. and *Xu, Zhai* et al. show strong dependencies of the support material used. [38–40] All three studies report weakly and strongly chemisorbed CO_2. This is also observable regarding the Fe/C-systems used in this study (Fig. 5A). Strongly chemisorbed CO_2, desorbed in the temperature range between

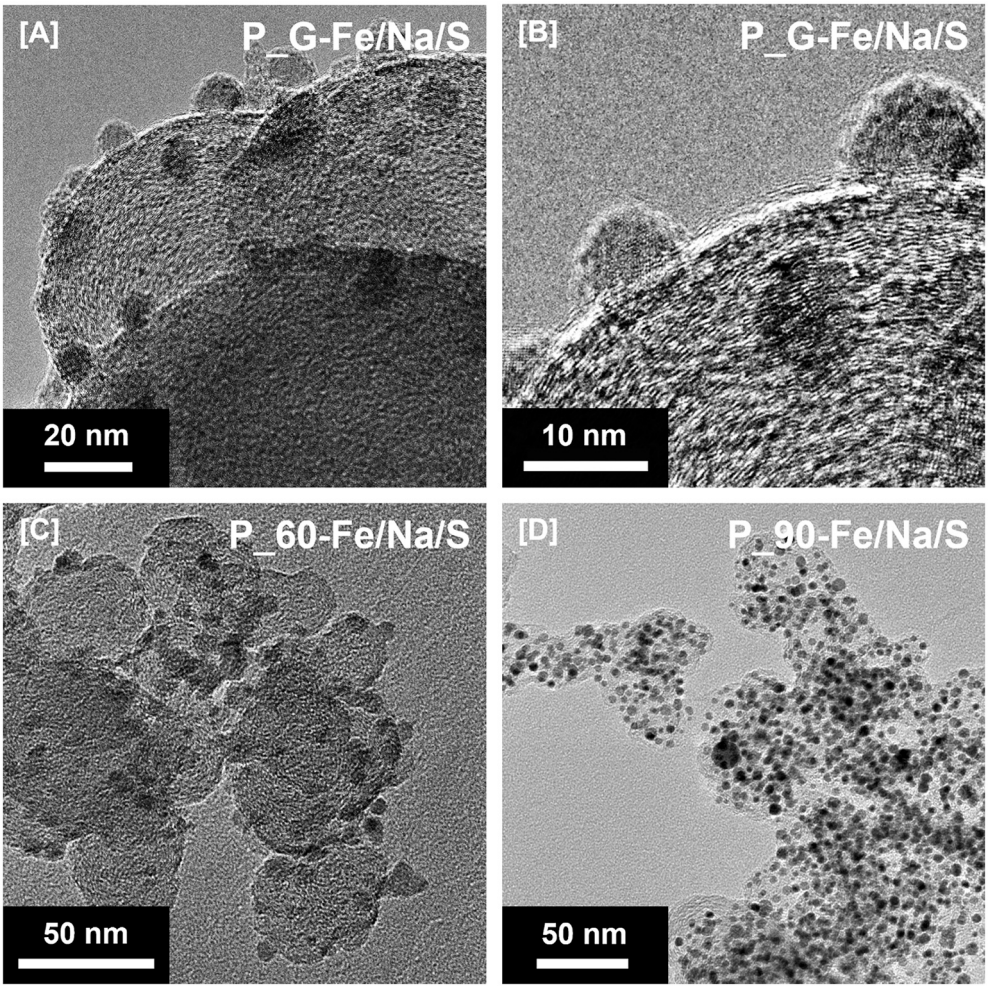

Fig. 4. Scanning transmission electron microscopy images of the pristine (A), (B) P_G-Fe/Na/S, (C) P_60-Fe/Na/S and (D) P_90-Fe/Na/S catalysts.

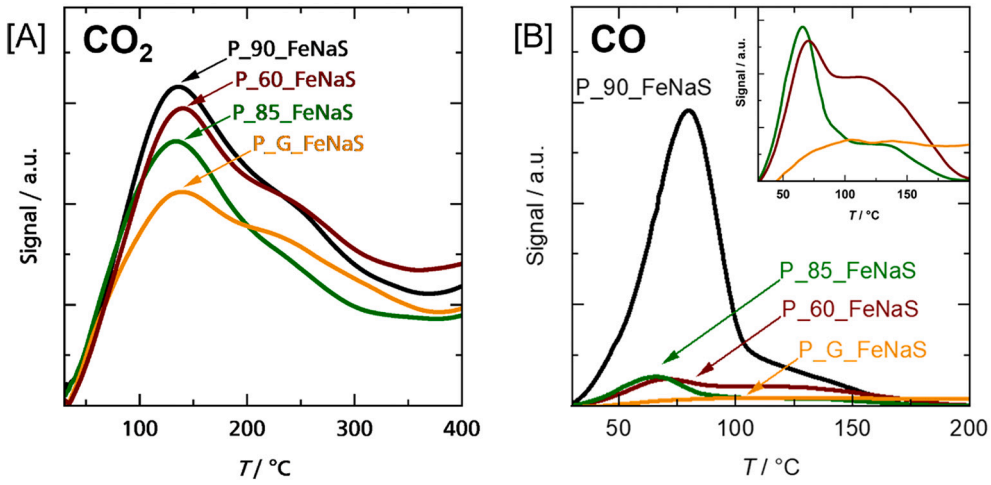

Fig. 5. (A) CO_2 and (B) CO-TPD of pristine carbon black supported Fe/Na/S catalysts.

200 °C and 300 °C, is related to the influence of highly basic Na_2O-species. [40] Desorption in lower temperature regions can also be assigned to CO_2 adsorbed on plain iron. [40] The resulting CO_2 binding strength of the carbon black supported catalysts lies between graphene oxide and silica supported iron systems. [38,39] In addition to CO_2-TPD, also CO-TPD was carried out, and shows the influence of alkali metals (Fig. 5B). [41] Strong CO chemisorption, caused by the already mentioned effect of Na_2O leads to a broad shoulder (100–150 °C) in addition to a desorption maximum at ~82 °C. This effect can be seen most significantly in case of P_90-Fe/Na/S. A reason for that is delivered by the static CO-chemisorption (Fig. S5) conducted prior the CO-TPD. P_90-Fe/Na/S includes, by far, the highest amount of reversible chemisorbed CO (4.6 $mmol_{CO}\ g_{Fe}^{-1}$, Fig. 3D). Due to the high amount of irreversible chemisorbed CO in case of P_60-Fe/Na/S (7.3 $mmol_{CO}\ g_{Fe}^{-1}$), the highest specific iron surface area (SSA_{Fe}) results (27.1 $m^2\ g_{Fe}^{-1}$). The large difference between reversible (0.6 $mmol_{CO}\ g_{Fe}^{-1}$) and irreversible chemisorbed CO might be caused by carbonylation and therefore iron leaching at low temperature (30 °C). [34] In contrast to that P_90-Fe/Na/S exhibits a SSA_{Fe} of 12.5 $m^2\ g_{Fe}^{-1}$ while P_G-Fe/Na/S (1 $m^2\ g_{Fe}^{-1}$) and P_35-Fe/Na/S (1.9 $m^2\ g_{Fe}^{-1}$) show much lower accessible iron surfaces. Table 1 gives a comprehensive summary of the characterization of the pristine catalysts.

Table 1
Summary of ICP-OES, TEM, N_2-physisorption, dynamic light scattering, oil adsorption and PZC characterization results of pristine Fe/Na/S supported on carbon black catalysts.

Support resp. Catalyst	Fe / wt %	Na / wt %	S / wt%	$d_{P,iron}$ / nm	SSA[a] / $m^2\ g^{-1}$	V_{Pore}^{b} / $cm^3\ g^{-1}$	$d_{P,CB}^{c}$ / nm	DBP number[c] / mL 100 g^{-1}
P_G resp. P_G-Fe/Na/S	9.7	0.62	0.15	7.2	54	0.09	51	96
P_35 resp. P_35-Fe/Na/S	9.5	0.63	0.10	7.6	72	0.24	31	42
P_60 resp. P_60-Fe/Na/S	9.9	0.64	0.15	6.5	113	0.22	21	114
P_85 resp. P_85-Fe/Na/S	9.7	0.93	0.12	7.5	150	0.26	16	48
P_90 resp. P_90-Fe/Na/S	9.9	0.45	0.27	3.7	343	0.48	14	95

[a]Specific surface area pristine catalyst. [b]Pore volume pristine catalyst. [c]Pristine carbon black catalyst support.

3.2. Influence of support on catalytic performance

Following the comprehensive characterization of the catalysts (Table 1) they were tested regarding their CO_2-FTS activity. Considering both CO_2 conversion (Fig. 6A) and CO yield (Fig. 6B), the five catalyst systems show considerable differences. While P_G-Fe/Na/S and P_35-Fe/Na/S show a FTS-typical start-up behaviour, with an increase of the conversion in the first 30 h from 22% and 15% to 25% and 21%, respectively, the catalyst supported on Printex 85 deactivates instantly after the start of the reaction. P_90-Fe/Na/S also shows a slight decrease in CO_2 conversion (X_{CO2}) over the course of the reaction time. Only P_60-Fe/Na/S shows a true steady state with an almost unchanged degree of CO_2 conversion of around 35% and a constant CO yield of 12.5%. The Printex G supported catalyst reaches a steady state in terms of CO yield ($Y_{CO,CO2}$) While P_35-Fe/Na/S and P_90-Fe/Na/S show largely identical $Y_{CO,CO2}$ curves with an increase from 12.5% to around 17%, P_85-Fe/Na/S reaches a maximum at 10 h TOS. Beyond activity, the product spectrum also differs between the individual catalyst supports (Fig. 6C and D). The catalyst supported on Printex 85 shows a hydrocarbon yield of only 1.4%, followed closely by P_35-Fe/Na/S (4.3%) and P_G-Fe/Na/S (6.5%). The catalytic performance of P_G-Fe/Na/S and P_35-Fe/Na/S differs only minimally, both in terms of the conversion and yield values as well as in relation to the product classes formed, with selectivities to methane of 62.7% and 63.0%, to alkanes of 24.0% and 23.1% to olefins of 6.2% and 8.5% and to alcohols of 7.0% and 9.2% with $Y_{HC,CO2}$ values of 15% and 20%, respectively, P_90-Fe/Na/S and P_60-Fe/Na/S show the highest FT yields. Strikingly, the two systems differ significantly in their product spectrum, which is reflected in both the α-values achieved and regarding the olefin fraction. The catalyst supported on Printex 90 with α-value of 0.32 tends to form significantly shorter carbon chains compared to the system supported on Printex 60 with 0.43. At the same time, almost exclusively saturated hydrocarbons are formed ($\sigma_{Met,CO2}$ = 48.8%, $\sigma_{Par,CO2}$ = 41.2%). Only P_60-Fe/Na/S, with an olefin content in the C_2-C_6 fraction of 40%, combined with the lowest selectivity to methane (24.6%) and the highest conversion of CO_2 (33.5%), shows true potential for the use as catalyst in the Fischer-Tropsch-to-olefins-reaction (FTO). This is also confirmed by the chain length distribution of the different product classes (Fig. S6) as all three substance classes, C_{2+} alkanes, alkenes and alcohols, exhibit maxima at low chain length between C_2 and C_4. Above a chain length of C_8, only

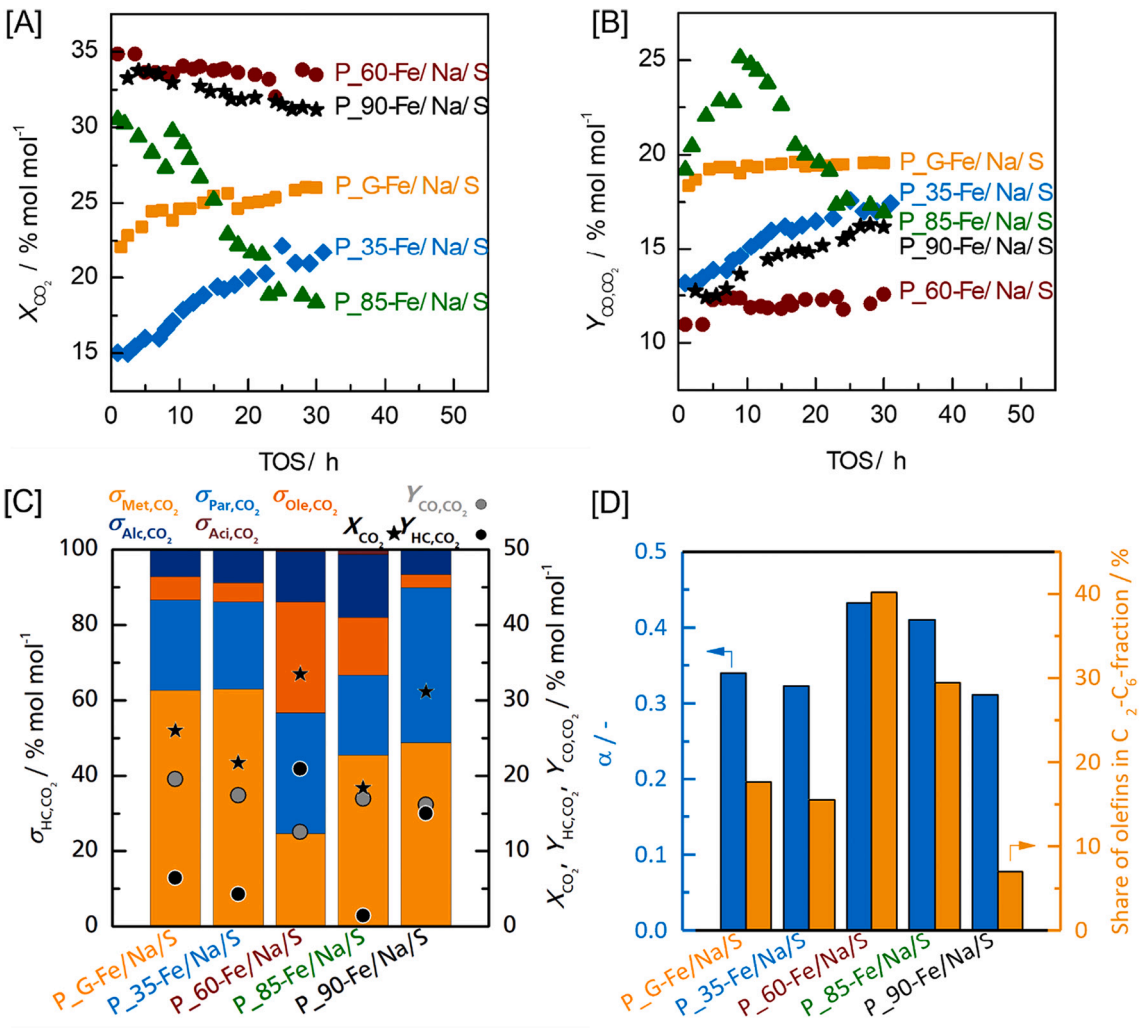

Fig. 6. Catalytic performance of Fe/CB catalysts promoted with Na and S using a stoichiometric H_2:CO_2-feed at 325 °C and 30 bar. (A) CO2 conversion (X_{CO2}) over time-on-stream and (B) CO yield ($Y_{CO,CO2}$) over 30 h TOS for the different support materials. (C) CO_2-coversion (black stars) as well as the yield of CO (grey circle) and hydrocarbons (black circles). The coloured columns represent the share of the different product classes in the total amount of produced hydrocarbons. Methane (light orange), C_{2+}-alkanes (light blue), alkenes (dark orange), alcohols (dark blue), acids (wine red). (D) α-value as well as olefin-amount in the C_2-C_6-fraction. All data points represent mean values of three measurements after 30 h TOS. (For interpretation of the references to colour in this figure legend, the reader is referred to the web version of this article.)

very negligible amounts of product are detected. Table 2 gives a comprehensive overview of the catalytic performance of all carbon black supported Fe/Na/S catalysts.

3.3. Characterization of the used catalysts

In order to explore changes in catalyst properties, post mortem characterization was carried out by N_2 physisorption, TEM and XRD. Regarding P_G-Fe/Na/S, P_35-Fe/Na/S and P_85-Fe/Na/S no changes in specific surface area can be observed. In contrast, SSA_{BET} of P_60-Fe/Na/S and P_90-Fe/Na/S decrease slightly (from 113 $m^2\ g^{-1}$ to 89 $m^2\ g^{-1}$ for P_60-Fe/Na/S and 343 $m^2\ g^{-1}$ to 294 $m^2\ g^{-1}$ for P_90-Fe/Na/S). A possible cause of this decrease is the sintering of the supported iron particles, as a lower number of particles with increased diameter leads to a lower specific surface area. Regarding the pore volumes according to the DFT method only in case of P_35-Fe/Na/S and P_60-Fe/Na/S a slight decrease can be observed (from 0.24 $cm^3\ g^{-1}$ to 0.19 $cm^3\ g^{-1}$ for P_35-Fe/Na/S and 0.22 $cm^3\ g^{-1}$ to 0.19 $cm^3\ g^{-1}$ for P_60-Fe/Na/S). The

Table 2
Catalytic performance of Fe/Na/S supported on different carbon blacks. All data points represent mean values of three measurements after 30 h TOS.

	X[a] CO_2 / %	Y[b] HC / %	Y[b] CO / %	σ[c]Methane / %	σ[c]Parafins / %	σ[c]Olefins / %	σ[c]Alcohols / %	σ[c]Acids / %	α / -	Share of olefins in C_2-C_6 fraction / %
P_G-Fe/Na/S	26	6	20	63	24	6	7	–	0.34	18
P_35-Fe/Na/S	22	4	17	63	23	5	9	–	0.32	16
P_60-Fe/Na/S	33	21	13	25	32	29	13	1	0.42	40
P_85-Fe/Na/S	18	1	17	45	21	15	17	1	0.41	29
P_90-Fe/Na/S	31	15	16	49	41	3	6	–	0.31	7

[a]CO_2 conversion; [b]yield of hydrocarbons (HC) and carbon monoxide (CO); [c]share of different product classes within the hydrocarbon fraction.

decrease in pore volume as a result of pore filling by long-chain FTS products is known from the literature, especially for cobalt-catalysed low-temperature FTS. [42] Due to the low average chain length of the products formed in the case of iron-catalysed HT FTS, this explanation is not convincing (Fig. S6). In addition, the decrease in pore volume would be more pronounced with an increasing rate of hydrocarbon formation, which is not the case here. It appears likely that the textural properties of the examined supports play a leading role in the activity of the corresponding FTS catalysts, as they significantly influence the resulting specific iron surface. The Printex G and Printex 35 supported catalysts have the lowest specific surface area, 54 $m^2\ g^{-1}$ and 72 $m^2\ g^{-1}$ respectively, and at the same time the lowest SSA_{Fe} (P_G-Fe/Na/S: 1 $m^2\ g_{Fe}^{-1}$) leading to a low catalytic activity. In contrast, a higher catalytic activity is observed in the case of P_60-Fe/Na/S and P_90-Fe/Na/S. These materials also include a higher SSA_{BET} of 113 $m^2\ g^{-1}$ and 343 $m^2\ g^{-1}$ resulting in a higher SSA_{Fe} of 27.1 $m^2\ g_{Fe}^{-1}$ and 12.5 $m^2\ g_{Fe}^{-1}$. Only P_85-Fe/Na/S represents an exception, as the specific surface area of 150 $m^2\ g^{-1}$ lies between that of P_60-Fe/Na/S and P_90-Fe/Na/S whereas this system shows low SSA_{Fe} (1.9 $m^2\ g_{Fe}^{-1}$) as well as the lowest FT activity.

In this context, the specific surface area of the carbon black and its degree of branching appear to be the key for the observed differences. A high specific surface area in combination with a high degree of branching appears to facilitate a good initial dispersion and high specific surface areas of FeO_x nanoparticles on Printex 60 as well as on Printex 90. High specific surface areas of the support, a high degree of branching as well as a high specific surface area of Fe nanoparticles all contribute to a large area of contact between the carbon black support and the FeO_x nanoparticles. This large contact area might facilitate the carburization of FeO_x in the first hours TOS to the FT active iron carbide phase, and thus the high hydrocarbon productivities of Fe/Na/S supported on Printex 60 and Printex 90. The other carbon black supports exhibit either a low degree of branching or comparatively low specific surface areas and do not facilitate the formation of well dispersed, accessible FeOx nanoparticles. In consequence, the area of contact between FeO_x and carbon black support might be much smaller, leading to a low degree of carburization with the large remaining fraction of iron oxide species accounting for a high selectivity to CO.

Oschatz et al. list sintering as the main reason for the deactivation of carbon-supported iron catalysts in the FTS. [15] TEM images of the used catalysts confirm the sintering of Fe nanoparticles over the course of 30 h of FTS (Fig. 7A, B). A broadening of the particle size distribution as well as a shift of the maximum of the distribution towards higher particle sizes is observed (Fig. 7C). This is reflected both in the mean value but also in the standard deviation. The largest increase of particle size is recorded in case of P_90-Fe/Na/S with an increase of 350% (Fig. 7D). Likewise, the averaged Fe particle size of P_60-Fe/Na/S increases by 299%. This behaviour correlates with the observations of *Torres Galvis* et al., who report increases in Fe particle size of 110–270% for an Al_2O_3-supported Fe/Na/S system after 120 h TOS. [23] It should be noted that in this study the time on stream was only 30 h, which led to a similar increase in Fe particle size. This observation is probably a consequence of different metal-support interactions, with the utilization of carbon black as a weakly interacting support leading to an increased sintering tendency. *Oschatz* et al., using carbon supports, also report significant increases in Fe particle sizes after 120 h or 140 h TOS. They increase on average to 25–28 nm and 16–18 nm, respectively, depending on the support material, [15,22] which translates to increases of 400% on CMK-3 and 280% on carbon black. It is also noticeable that Fe particle growth seems to correlate with catalytic activity: particle growth is significantly less pronounced regarding P_G-Fe/Na/S, P_35-Fe/Na/S and P_85-/Fe/Na/S, correlating directly with the lower FT activity of these systems.

According to XRD measurements of the used catalysts two significant differences are observed (Fig. 7E, F). Additional weakly pronounced reflexes appear in the range of 40° / 2θ to 60° / 2θ. Although challenging to assign to individual Fe phases, most likely iron carbides such as the Eckstrom-Adcock carbide (Fe_3C_7), cementite (Θ-Fe_3C) or a poorly defined iron carbide structure (Fe_xC_y) are responsible for these new reflexes. [43] Furthermore, it is striking that the iron oxide reflexes at 30° / 2θ, 35° / 2θ, 43° / 2θ, 57° / 2θ and 63° / 2θ are clearly narrower and more intense in the case of the used catalyst. Due to the intensity ratios, a phase pure FeO_x species is still not present, however, the ratios known from Fe_3O_4 are clearly approached. Possible reasons for this observation are the transformation of FeO to Fe_3O_4, Fe^0 as well as FeC_x, while the narrowing of reflexes can be attributed to the growth of the crystallites, [36] thereby indicating sintering.

In summary, P_60-Fe/Na/S emerges from the support variation as the most suitable industrial carbon black. Accordingly, this material is used as the catalyst support for the long-term stability test.

3.4. Long-term stability testing

The Printex 60 supported system was additionally tested for its long-term-stability over 170 h TOS (Fig. 8A, B). The conversion of CO_2 reaches a steady state of about 30% directly with the setting of the operating conditions after the preconditioning of the catalyst at 48 h TOS. Over the entire test period of 170 h TOS, X_{CO2} fluctuates only within the range of 28.2% to 31.5%, while no deactivation is observed. A similar behaviour for K/Mn/Fe catalysts on nitrogen-doped CNTs is reported by *Kangvansura* et al.. Following the first 40 h of TOS, which roughly corresponds to the duration of the preconditioning performed in the present work, they report steady-state CO_2 conversions of 25.4% to 31.8% for the following 20 h of TOS at 25 bar and 360 °C. The group attributes the deactivation during the induction period to the growth of the iron particles. [43] It should be noted that catalyst deactivation might also be caused by re-oxidation of FT-active iron carbide species to FeO_x species. However, in case of CO_2 hydrogenation to olefins this connection is non-trivial, as the presence of iron oxide species are integral to the desired reaction pathway as they catalyse the conversion of CO_2 to CO via the RWGS equilibrium. As CO_2 conversion as well as the yield of CO and hydrocarbons remains stable over 170 h TOS, we assume that after preconditioning a steady state between iron carburization and oxidation is established which results in a constant ratio of FeO_x and FeC_x species. The steady-state yields of hydrocarbons and CO are ~16% in the case of $Y_{HC,CO2}$ and ~ 14% for $Y_{CO,CO2}$, corresponding to selectivities of 53% and 46%, respectively. Thus, the CO selectivity of 48.5% published by *Kangvansura* et al. on a Mn/Fe/NCNT system is achieved. [43] Significant changes over the reaction time occur exclusively with regard to the products formed. In this context, from 80 h TOS, an increase in the proportion of methane from 22% to 38% can be observed. At the same time, the proportion of C_{2+}-alkanes decreases from 23% at the beginning to 16%. Alkenes and alcohols show similar trends. Starting from initial values of 33% and 15%, respectively, both proportions increase to 42% and 18%, respectively, up to a TOS of 62 h, and then decrease.

Between 100 h and 175 h TOS, both values fluctuate in very narrow ranges between 31% and 33% in the case of the alkenes and between 13% and 14% in the case of the alcohols. Consequently, regarding the whole reaction time, no significant changes for these to product classes exist. The observations described are also reflected in the chain growth probabilities and olefin fractions in the C_2-C_6 fraction shown in Fig. 5B. As a result of the increasing fraction of methane formed, the chain growth probability drops slightly from 0.48 to 0.45. However, it should be noted that the plotted α-values are subject to a considerable scatter in the range of 0.5 to 0.43. At the same time, due to decreasing alkane-content, the share of olefins on the C_2-C_6 fraction rises steadily from 42% to almost 50% from a TOS of 90 h onwards. At that point additionally studies are necessary to explain the changes regarding the product selectivities.

4. Conclusion

Within the present study, iron-based Fischer-Tropsch catalysts were

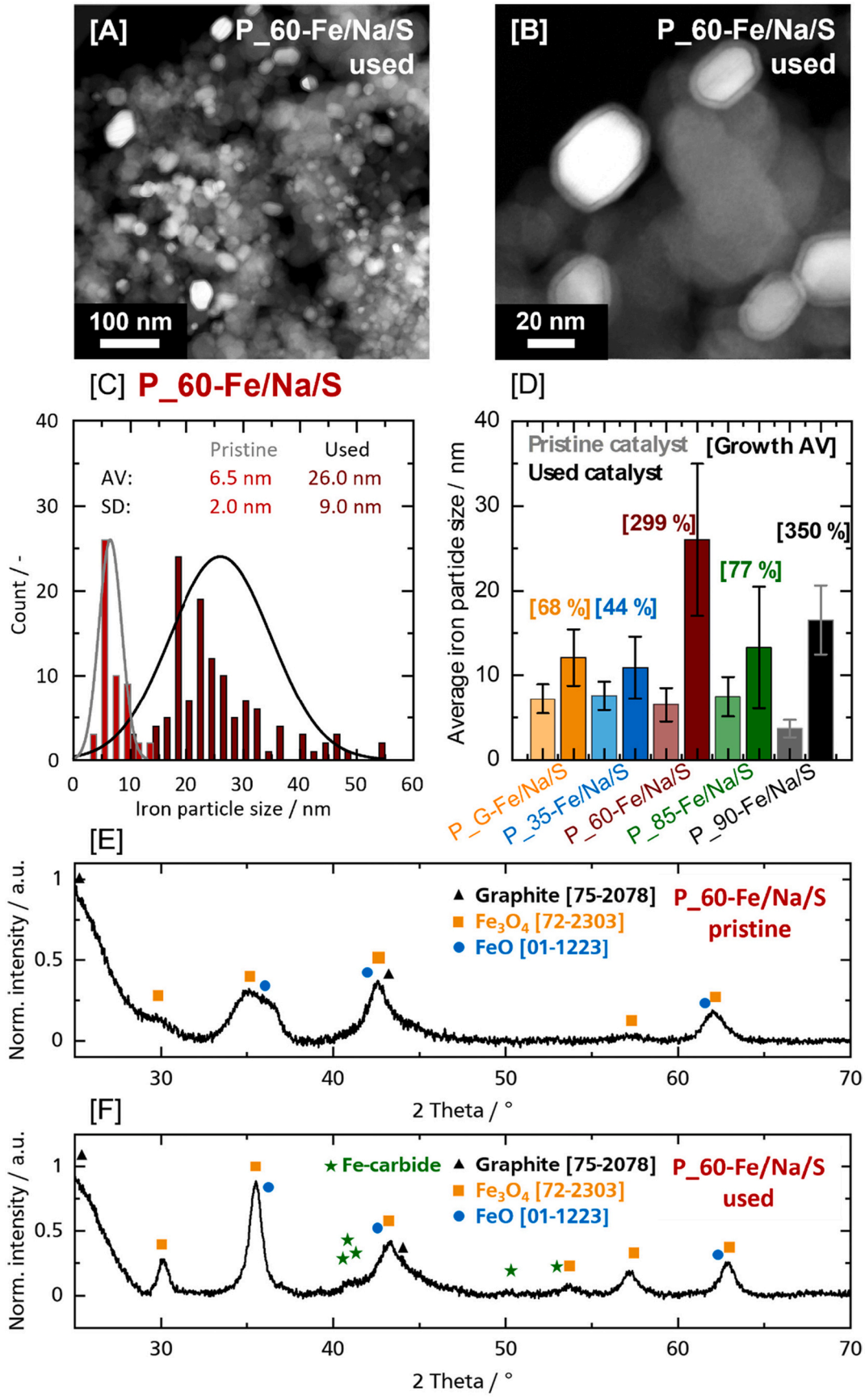

Fig. 7. Characterization of the used catalysts after 30 h TOS. (A), (B) TEM micrographs of P_60-Fe/Na/S after 30 h TOS. (C) Particle size distributions of P_60-Fe/Na/S before and after 30 h TOS. (D) Average particle sizes before and after 30 h Fischer-Tropsch synthesis of all carbon black supported Fe/Na/S catalysts. (E), (F) XRD of pristine and used P_60-Fe/Na/S.

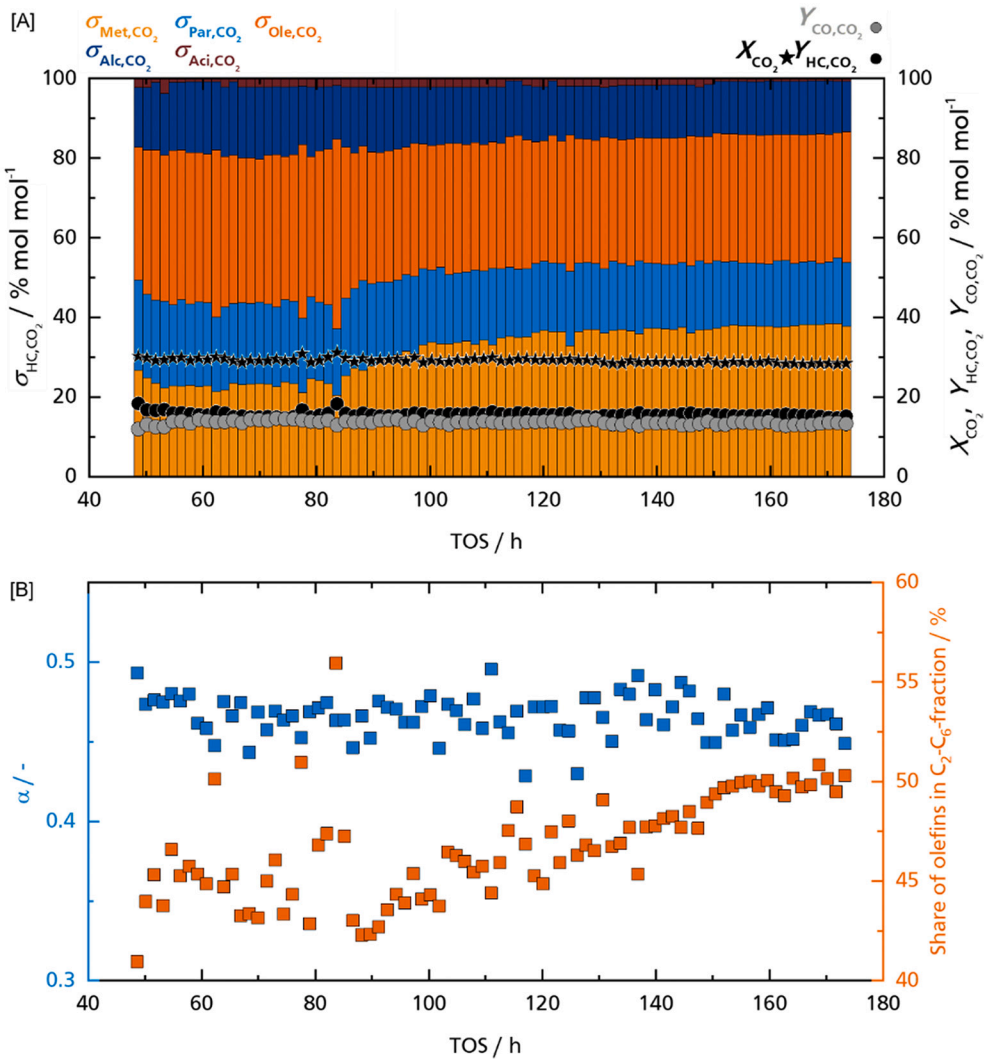

Fig. 8. Catalytic performance of Fe/CB catalyst promoted with sodium and sulfur using a stoichiometric H_2:CO_2-feed at 325 °C and 30 bar. (A) CO_2-conversion (black stars) and yields of CO_2 (grey circle) and hydrocarbons (black circles). The coloured columns represent the share of the different product classes in the total amount of produced hydrocarbons. Methane (light orange), C_{2+}-alkanes (light blue), alkenes (dark orange), alcohols (dark blue), acids (wine red). (B) α-value and olefin-amount in the C_2-C_6-fraction over 175 h TOS. (For interpretation of the references to colour in this figure legend, the reader is referred to the web version of this article.)

prepared with sodium and sulfur promoters supported on five industrially available, beaded carbon blacks. The carbon blacks exhibited different structural parameters, with specific surface areas ranging from 36 $m^2\ g^{-1}$ to 380 $m^2\ g^{-1}$. As a result of testing these systems regarding their suitability as CO_2-FTS-catalysts with the target product short-chain olefins, clear correlations emerge between the structure of the materials and their catalytic activity. Thus, the combination of aggregates with a high degree of branching and a specific surface area in the range of 150 $m^2\ g^{-1}$ proves to be desirable. Using the most promising system (X_{CO2} = 35%, $\sigma_{C2\text{-}C6\text{-}Ole,CO2}$ = 40%), the long-term stability of the Fe/C catalysts over 170 h TOS was demonstrated, whereas no decrease in CO_2 conversion was observed. In this study we could demonstrate that inexpensive, industrial available beaded carbon blacks can be utilized as supports to prepare easy-to-handle Fe based FTS catalysts exhibiting high stability along with similar catalytic activity and selectivity compared to considerably more expensive carbon nanomaterials such as CNT's.

List of abbreviations

Aci	acids
Alc	alcohols
CB	carbon black
CMK-3	ordered mesoporous carbon
CNT	carbon nano tubes
DBP	dibutyl phtalate
DFT	density functional theory
FID	flame ionisation detector
FT-IR	fourier-transform infrared
FTO	fischer-tropsch-to-olefins
FTS	fischer-tropsch-synthesis
GC	gas chromatograph
GHSV	gas hourly space velocity
STEM	scanning transmission elektron microskopy
ICP-OES	optical emission spectroscopy with inductiv coupled plasma
IWI	incipient wetness impregnation
HC	hydrocarbons
MBET	multi-point brunauereEmmett-teller-methode
Met	methane
MTO	methanol to olefins
O/P	olefin−/paraffin ratio
OEC	orion engineered carbons
Ole	olefins
Par	paraffins
SMSI	strong metal support interaction
TCD	thermal conductivity detector
TPD/TPR	temperature programmed desorption / reduction
(R)WGS	(reverse) watergas-shift-reaction
XRD	x-ray diffraction

List of symbols

α	chain growth propability, –
$d_{P,cCB/iron}$	carbon black / iron diameter, nm
$Q_{CO,Ads,rev/irrev}$	quantity of reversible / irreversible adsorbed CO, mmol g_{Fe}^{-1}
$S_{p,r}$	selecivity to product p from reactant r, mol mol^{-1}
$\sigma_{HC,r}$	share of hydrocarbon HC related to all HC's, mol mol^{-1}
$S_{HC,r}$	selecivity to hydrocarbon HC from reactant r, mol mol^{-1}
SSA_{BET}	specific surface area using BET-method, $m^2\ g^{-1}$
TOS	time on stream, h
V_{Pore}	pore volume, $cm^3\ g^{-1}$
$w_{Fe,Kat}$	weight fraction of iron related to total catalyst mass, g g^{-1}
X_r	conversion of reactant r, mol mol^{-1}
$Y_{p,r}$	yield of product p out of reactant r, mol mol^{-}

Declaration of Competing Interest

The authors declare that they have no known competing financial interests or personal relationships that could have appeared to influence the work reported in this paper.

Data availability

Data will be made available on request.

Acknowledgements

Stephan Schultheis acknowledges a fellowship from the Darmstadt Graduate School of Excellence Energy Science and Engineering. Felix Herold acknowledges a fellowship within the Walter-Benjamin-program of the Deutsche Forschungsgemeinschaft (DFG, German Research Foundation, project number 471263729). The authors acknowledge funding from DFG within CRC 1487 (Iron, upgraded!; project number 443703006). Orion Engineered Carbons is acknowledged for providing carbon black samples.

Appendix A. Supplementary data

Supplementary data to this article can be found online at https://doi.org/10.1016/j.catcom.2023.106622.

References

[1] R. Schmidt, K. Griesbaum, A. Behr, D. Biedenkapp, H.-W. Voges, D. Garbe, C. Paetz, G. Collin, D. Mayer, H. Höke, Hydrocarbons, in: Ullmann's Encyclopedia of Industrial Chemistry, Wiley-VCH Verlag GmbH & Co. KGaA, Weinheim, Germany, 2000, pp. 1–74.
[2] Verband der Chemischen Industrie (VCI) e. V, Auf einen Blick - Chemische Industrie 2020, Frankfurt am Main, 2020.
[3] R. Dittmeyer, M. Klumpp, P. Kant, G. Ozin, Crowd oil not crude oil, Nat. Commun. 10 (2019) 1818, https://doi.org/10.1038/s41467-019-09685-x.
[4] S. De, A. Dokania, A. Ramirez, J. Gascon, Advances in the design of heterogeneous catalysts and thermocatalytic processes for CO 2 utilization, ACS Catal. 10 (2020) 14147–14185, https://doi.org/10.1021/acscatal.0c04273.
[5] M. de Smet, M. Linder, R. Koopmans, et al., A Circular Economy for Plastics Insights from Research and Innovation to Inform Policy and Funding Decisions, European Commission, Directorate-General for Research and Innovation, 2019, https://doi.org/10.2777/269031.
[6] O. Dogu, M. Pelucchi, R. van de Vijver, P.H. van Steenberge, D.R. D'hooge, A. Cuoci, M. Mehl, A. Frassoldati, T. Faravelli, K.M. van Geem, The chemistry of chemical recycling of solid plastic waste via pyrolysis and gasification: state-of-the-art, challenges, and future directions, Prog. Energy Combust. Sci. 84 (2021), 100901, https://doi.org/10.1016/j.pecs.2020.100901.
[7] G.W. Coates, Y.D.Y.L. Getzler, Chemical recycling to monomer for an ideal, circular polymer economy, Nat. Rev. Mater. 5 (2020) 501–516, https://doi.org/10.1038/s41578-020-0190-4.
[8] A. Lechleitner, D. Schwabl, T. Schubert, M. Bauer, M. Lehner, Chemisches Recycling von gemischten Kunststoffabfällen als ergänzender Recyclingpfad zur Erhöhung der Recyclingquote, Österr Wasser- und Abfallw 72 (2020) 47–60, https://doi.org/10.1007/s00506-019-00628-w.
[9] S. Flamme, J. Hanewinkel, P. Quicker, K. Weber, Energieerzeugung aus Abfällen Stand und Potenziale in Deutschland bis 2030, Umweltbundesamt, 2018.
[10] S.W. Han, J.J. Lee, D. Tokmurzin, S.H. Lee, J.Y. Nam, S.J. Park, H.W. Ra, T.-Y. Mun, S.J. Yoon, S.M. Yoon, J.H. Moon, J.G. Lee, Y.-M. Kim, Y.W. Rhee, M. W. Seo, Gasification characteristics of waste plastics (SRF) in a bubbling fluidized bed: effects of temperature and equivalence ratio, Energy 238 (2022), 121944, https://doi.org/10.1016/j.energy.2021.121944.
[11] M. Materazzi, R. Taylor, P. Cozens, C. Manson-Whitton, Production of BioSNG from waste derived syngas: pilot plant operation and preliminary assessment, Waste Manag. 79 (2018) 752–762, https://doi.org/10.1016/j.wasman.2018.08.031.
[12] M.E. Dry, The Fischer–Tropsch (FT) synthesis processes, in: G. Ertl, H. Knözinger, F. Schüth, J. Weitkamp (Eds.), Handbook of Heterogeneous Catalysis, 2nd ed., Wiley-VCH, Weinheim, 2008, pp. 2965–2994.
[13] J. Wang, Z. You, Q. Zhang, W. Deng, Y. Wang, Synthesis of lower olefins by hydrogenation of carbon dioxide over supported iron catalysts, Catal. Today 215 (2013) 186–193, https://doi.org/10.1016/j.cattod.2013.03.031.
[14] F. Jiang, M. Zhang, B. Liu, Y. Xu, X. Liu, Insights into the influence of support and potassium or sulfur promoter on iron-based Fischer–Tropsch synthesis: understanding the control of catalytic activity, selectivity to lower olefins, and catalyst deactivation, Catal. Sci. Technol. 7 (2017) 1245–1265, https://doi.org/10.1039/C7CY00048K.
[15] M. Oschatz, W.S. Lamme, J. Xie, A.I. Dugulan, K.P. de Jong, Ordered mesoporous materials as supports for stable iron catalysts in the fischer-tropsch synthesis of lower olefins, ChemCatChem 8 (2016) 2846–2852, https://doi.org/10.1002/cctc.201600492.
[16] V.K. Jones, L.R. Neubauer, C.H. Bartholomew, Effects of crystallite size and support on the carbon monoxide hydrogenation activity/selectivity properties of iron/carbon, J. Phys. Chem. 90 (1986) 4832–4839, https://doi.org/10.1021/j100411a023.
[17] G. Yu, B. Sun, Y. Pei, S. Xie, S. Yan, M. Qiao, K. Fan, X. Zhang, B. Zong, Fe(x)O(y)@C spheres as an excellent catalyst for Fischer-Tropsch synthesis, J. Am. Chem. Soc. 132 (2010) 935–937, https://doi.org/10.1021/ja906370b.
[18] R.M.M. Abbaslou, A. Tavassoli, J. Soltan, A.K. Dalai, Iron catalysts supported on carbon nanotubes for Fischer–Tropsch synthesis: Effect of catalytic site position, Appl. Catal., A 367 (2009) 47–52, https://doi.org/10.1016/j.apcata.2009.07.025.
[19] M.C. Bahome, L.L. Jewell, K. Padayachy, D. Hildebrandt, D. Glasser, A.K. Datye, N. J. Coville, Fe-Ru small particle bimetallic catalysts supported on carbon nanotubes for use in Fischer–Tröpsch synthesis, Appl. Catal. A 328 (2007) 243–251, https://doi.org/10.1016/j.apcata.2007.06.018.
[20] H.M. Torres Galvis, A.C. Koeken, J.H. Bitter, T. Davidian, M. Ruitenbeek, A. I. Dugulan, K.P. de Jong, Effects of sodium and sulfur on catalytic performance of supported iron catalysts for the Fischer–Tropsch synthesis of lower olefins, J. Catal. 303 (2013) 22–30, https://doi.org/10.1016/j.jcat.2013.03.010.
[21] S.M. Lama, J.L. Weber, T. Heil, J.P. Hofmann, R. Yan, K.P. de Jong, M. Oschatz, Tandem promotion of iron catalysts by sodium-sulfur and nitrogen-doped carbon layers on carbon nanotube supports for the Fischer-Tropsch to olefins synthesis, Appl. Catal., A 568 (2018) 213–220, https://doi.org/10.1016/j.apcata.2018.09.016.
[22] M. Oschatz, N. Krans, J. Xie, K.P. de Jong, Systematic variation of the sodium/sulfur promoter content on carbon-supported iron catalysts for the Fischer–Tropsch to olefins reaction, J. Energy Chem. 25 (2016) 985–993, https://doi.org/10.1016/j.jechem.2016.10.011.
[23] H.M. Torres Galvis, J.H. Bitter, T. Davidian, M. Ruitenbeek, A.I. Dugulan, K.P. de Jong, Iron particle size effects for direct production of lower olefins from synthesis gas, J. Am. Chem. Soc. 134 (2012) 16207–16215, https://doi.org/10.1021/ja304958u.
[24] F. Jiang, B. Liu, S. Geng, Y. Xu, X. Liu, Hydrogenation of CO 2 into hydrocarbons: enhanced catalytic activity over Fe-based Fischer–Tropsch catalysts, Catal. Sci. Technol. 8 (2018) 4097–4107, https://doi.org/10.1039/C8CY00850G.
[25] M. Thommes, K. Kaneko, A.V. Neimark, J.P. Olivier, F. Rodriguez-Reinoso, J. Rouquerol, K.S. Sing, Physisorption of gases, with special reference to the evaluation of surface area and pore size distribution (IUPAC Technical Report), Pure Appl. Chem. 87 (2015) 160, https://doi.org/10.1515/pac-2014-1117.
[26] D24 Committee, Test Method for Carbon BlackOil Absorption Number (OAN), ASTM International, West Conshohocken, PA.
[27] Orion Engineered Carbons, Specialty Carbon Blacks: Technical Data Europe, 2016.
[28] D24 Committee, Test Methods for Carbon BlackAsh Content, ASTM International, West Conshohocken, PA.
[29] J. Figueiredo, M. Pereira, M. Freitas, J. Órfão, Modification of the surface chemistry of activated carbons, Carbon 37 (1999) 1379–1389, https://doi.org/10.1016/S0008-6223(98)00333-9.
[30] J.L. Figueiredo, M.F.R. Pereira, M.M.A. Freitas, J.J.M. Órfão, Characterization of active sites on carbon catalysts, Ind. Eng. Chem. Res. 46 (2007) 4110–4115, https://doi.org/10.1021/ie061071v.
[31] F. Herold, J. Gläsel, B.J.M. Etzold, M. Rønning, Can temperature-programmed techniques provide the gold standard for carbon surface characterization? Chem. Mater. 34 (2022) 8490–8516, https://doi.org/10.1021/acs.chemmater.2c02449.
[32] K. Jurkiewicz, M. Pawlyta, A. Burian, Structure of Carbon Materials Explored by Local Transmission Electron Microscopy and Global Powder Diffraction Probes, C 4, 2018, p. 68, https://doi.org/10.3390/c4040068.
[33] H. Yan, J. Zhang, C. You, Z. Song, B. Yu, Y. Shen, Influences of different synthesis conditions on properties of Fe3O4 nanoparticles, Mater. Chem. Phys. 113 (2009) 46–52, https://doi.org/10.1016/j.matchemphys.2008.06.036.
[34] C.-L. Liu, Y.-K. Peng, S.-W. Chou, W.-H. Tseng, Y.-J. Tseng, H.-C. Chen, J.-K. Hsiao, P.-T. Chou, One-step, room-temperature synthesis of glutathione-capped iron-oxide

nanoparticles and their application in in vivo T1-weighted magnetic resonance imaging, Small 10 (2014) 3962–3969, https://doi.org/10.1002/smll.201303868.
[35] K.D.M. Harris, M. Tremayne, B.M. Kariuki, Contemporary advances in the use of powder X-ray diffraction for structure determination, Angew. Chem. Int. Ed. 40 (2001) 1626–1651, https://doi.org/10.1002/1521-3773(20010504)40:9<1626:AID-ANIE16260>3.0.CO;2-7.
[36] L.M. Chew, P. Kangvansura, H. Ruland, H.J. Schulte, C. Somsen, W. Xia, G. Eggeler, A. Worayingyong, M. Muhler, Effect of nitrogen doping on the reducibility, activity and selectivity of carbon nanotube-supported iron catalysts applied in CO2 hydrogenation, Appl. Catal., A 482 (2014) 163–170, https://doi.org/10.1016/j.apcata.2014.05.037.
[37] W. Ma, E.L. Kugler, J. Wright, D.B. Dadyburjor, Mo−Fe catalysts supported on activated carbon for synthesis of liquid fuels by the Fischer−Tropsch process: effect of Mo addition on reducibility, activity, and hydrocarbon selectivity, Energy Fuel 20 (2006) 2299–2307, https://doi.org/10.1021/ef0602372.
[38] Y. Cheng, J. Lin, K. Xu, H. Wang, X. Yao, Y. Pei, S. Yan, M. Qiao, B. Zong, Fischer–tropsch synthesis to lower olefins over potassium-promoted reduced graphene oxide supported iron catalysts, ACS Catal. 6 (2016) 389–399, https://doi.org/10.1021/acscatal.5b02024.
[39] L. Xu, Q. Wang, D. Liang, X. Wang, L. Lin, W. Cui, Y. Xu, The promotions of MnO and K2O to Fe/silicalite-2 catalyst for the production of light alkenes from CO2 hydrogenation, Appl. Catal., A 173 (1998) 19–25, https://doi.org/10.1016/S0926-860X(98)00141-0.
[40] Y. Xu, P. Zhai, Y. Deng, J. Xie, X. Liu, S. Wang, D. Ma, Highly selective olefin production from CO 2 hydrogenation on Iron catalysts: a subtle synergy between manganese and sodium additives, Angew. Chem. 132 (2020) 21920–21928, https://doi.org/10.1002/ange.202009620.
[41] K. Cheng, V.V. Ordomsky, M. Virginie, B. Legras, P.A. Chernavskii, V.O. Kazak, C. Cordier, S. Paul, Y. Wang, A.Y. Khodakov, Support effects in high temperature Fischer-Tropsch synthesis on iron catalysts, Appl. Catal., A 488 (2014) 66–77, https://doi.org/10.1016/j.apcata.2014.09.033.
[42] F. Pöhlmann, Zusammenspiel von chemischer Reaktion und Porendiffusion bei der kobaltkatalysierten Fischer-Tropsch-Synthese unter Einsatz von CO2-haltigem Synthesegas. Dissertation, Bayreuth, 2017.
[43] P. Kangvansura, L.M. Chew, C. Kongmark, P. Santawaja, H. Ruland, W. Xia, H. Schulz, A. Worayingyong, M. Muhler, Effects of potassium and manganese promoters on nitrogen-doped carbon nanotube-supported iron catalysts for CO 2 hydrogenation, Engineering 3 (2017) 385–392, https://doi.org/10.1016/J.ENG.2017.03.013.